

Novel optofluidic refractometer based on wedge interferometry for handheld testing devices

Noha Gaber,^{1,*}

¹*Center for Nanotechnology, Zewail City of Science and Technology, Sheikh Zayed District, 6th of October City, Giza, 12588, Egypt*

**Corresponding author: ngaber@zewailcity.edu.eg*

Abstract

Interferometric methods are known for their high sensitivity for biochemical optical sensing, but on the expense of their large size. By using wedge interferometry, the size can be drastically reduced while maintaining adequate detection capabilities. In this article, a miniaturized refractometer based on this interferometer type is demonstrated to be able to achieve Sensitivity of 1.66×10^{-5} RIE/ μm and Detection Limit of 8.7×10^{-5} RIE for bulk refractometry of glucose aqueous solution. The device consists of two semitransparent mirrors made of glass slide coated by sputtered Aluminum thin film, enclosing a tapered frame that maintains one mirror slightly tilted with respect to the other, and simultaneously encloses the liquid under test. This structure causes interference pattern that depends on the refractive index of the test liquid when illuminated by a collimated laser beam. Analytical modeling is developed for the structure, from which a very promising estimation of the sensitivity is evaluated that exceeds the state-of-the-art for volume refractometry, and can be achieved upon using microfabrication techniques. Numerical simulations are also presented for principle validation. The proposed novel device opens a new avenue for optofluidic detection and is very suitable for point-of-care-testing and handheld devices due to its compact size, simple and cheap fabrication.

Keywords: interferometry for detection; miniaturized refractometer; optofluidic sensor; refractive index measurement; wedge interferometer

1. Introduction

Bio-photonic sensors and biochemical optical sensors are the vital parts for point-of-care testing (POCT) devices. Such POCT devices are attracting huge interest as they provide fast performance, low cost, less sample size and reagents, and most importantly, portability which makes them available almost everywhere. POCT technology is even extending to other applications beside human health diagnostics, including food quality control, water quality monitoring, and pathogen detection [1]. Almost all of these detection mechanisms are in fact relying on chemical detection. One of the most fundamental chemical detection instruments is refractometer, which is usually found in almost every chemical analysis lab. The optical refractometry characterization technique is well-known of being label-free and real-time method for

identifying dielectric materials by measuring their refractive index (RI); thereby, it has various industrial, environmental, and biomedical applications. With the wide interest in microfluidics and lab-on-a-chip systems, several attempts have been done trying to integrate various optical detection techniques on-chip [2]; leading to the advent of what is called 'optofluidics' [3]. A lot of refractometry methods has the possibility to be easily included into the micro-size system, but most of them still need external bulky expensive equipment such as optical spectrum analyzer or surface enhanced Raman spectrometer [4], which are still challenging to be miniaturized. But using spatial interferometry techniques evade using such bulky equipment, which will be investigated in this work.

Interferometry techniques generally are trusted for their detection and sensing capabilities; not only in chemical detection techniques, but also in various fields such as optometry, velocimetry, astronomy, quantum mechanics, spectroscopy and its applications in chemistry and material science. Even it has been trusted, since long time ago, to be the sensitive enough technique for detecting the extremely tiny strains in space indicating gravitational waves; which is considered the experimental prove for Einstein's relativity theory [5]. Several decades later, specifically in 2016, gravitational waves have been successfully detected by the LIGO (Laser Interferometer Gravitational-Wave Observatory), a Michelson interferometer with two arms of 4 km length [6]. The secret behind the high sensitivity of interferometric methods is that it has the capability of 'building up' the sensitivity. This is achieved by increasing the optical path of the interferometer arms, thereby the phase difference of light accumulates the longer the beam travels [7]. But inherently, increasing the arms' length implies large size apparatus to provide the high sensitivity. This is not necessarily the case with the wedge interferometry configuration introduced in this work. In wedge interferometry, the slope of one mirror with respect to the other also controls this issue, as will be demonstrated in details in this article. Overcoming the large size is of great benefit for hand-held measuring devices and POCT, while using the interferometer as a refractometer of fluidic samples guarantees high sensitivity. Previous refractometers based on spatial interferometric methods found in literature are based on Young interferometer configuration [8-11], which necessitates large distance between the interferometer output and the display to be able to resolve the small phase difference between the two branches. There are other configurations based on Mach-Zehnder Interferometers where this drawback is less pronounced [12, 13], but usually Young interferometers achieve better performance. The spatial interferometric method holds the highest sensitivity record for both surface refractometry and volume refractometry. In surface refractometry, the interaction with the sample is achieved only by the evanescent part of the electromagnetic light wave; like surface plasmon resonance techniques [14], integrated dielectric waveguides [15], optical resonators supporting Whispering Gallery Modes, such as ring resonators [16] and spherical resonators [17]. The resolution of these techniques is superior, which are capable of detecting refractive index changes (Δn) as small as 9×10^{-9} RIU in case of Young interferometer configuration [8]. But on the other hand, they are vulnerable to surface contamination; beside having small interaction length with the sample as the evanescent field usually can reach few hundreds of nanometers only. This small interaction length makes it not efficient in some applications such as testing biological cells as they can't penetrate their membrane. On the other hand, the advantage of the volume refractometry (also known sometimes by bulk refractometry) is that the light waves pass directly through the sample under test, increasing the depth of

interaction; beside being more robust against contamination and also has the ability to penetrate and probe the entire sample, not its surface only. But these advantages come on the expense of resolution as it is usually in the range of 10^{-7} RIU only, achieved also by interferometric methods. Young interferometer formed by simple double slit configuration gave sensitivity of 2×10^{-6} RIU/ μm with Δn of 9.67×10^{-7} RIU [9], while a Y-branch on-chip configuration could give sensitivity of 2.5×10^{-7} RIU/ μm and Δn of 1×10^{-7} RIU [11]. Another advantage of spatial interferometric method beside its high sensitivity is that it usually don't involve large sophisticated equipment such as spectrometers, as they depend on detecting spatial interference fringes that can be simply imaged by CCD/CMOS cameras that also allows automated digital readout. That make it very attractive for POCT devices, if a total compact size could be realized.

In this work, a compact size, cheap and simple refractometer based on wedge interferometry is proposed. This configuration is novel in the field of refractometry applications, as wedge fringes technique hasn't been previously used except for plate or film thickness determination [18]. Our device consists of a fluidic chamber with a designed tilt angle between two semi-reflecting mirrors to form the interference fringes. Upon recording these fringes' shift with changing the liquid filling the chamber, the RI difference between the test liquid and a reference one can be determined. The design, simulation and experimental demonstration of such device is presented below.

2. Methodology

2.1. Proposed structure

The proposed structure consists of a Fabry–Pérot cavity with variable gap thickness. This can be manufactured on-chip by two mirrors -either Bragg mirrors [19, 20] or metallic mirrors- in front of each other with one of them tilted with respect to the other by a designed tilting angle. The microfabrication techniques by photolithography and etching processes can control small and accurate dimensions in the micro range to achieve small tilt angle that achieves high sensitivity. But even if microfabrication techniques are not available, a simple device like that indicated by the cross section schematic in Figure 1 can achieve good sensitivity. The proposed device consists of a fluidic chamber or frame with a variable height made of Polydimethylsiloxane (PDMS) polymer. It has a height of (d) from one side and a height of ($d + t$) from the other side. This frame is sandwiched between two semi reflecting mirrors. Due to the varying height of the frame, one mirror is tilted by an angle α with respect to the other mirror. Input/output fluidic tubes are connected to deliver the liquid under test to the device.

To understand the principle of operation, the structure can be considered as a Fabry–Pérot resonator but with varying length (ℓ) enclosed between the two mirrors. When a collimated monochromatic light of certain wavelength (λ) is incident on this varying length resonator, the cavity length ℓ at some regions will be equivalent to multiples of $\lambda/2$ forming constructive interference and hence a bright fringe at the output due to perfect phase matching between the multiply reflected rays between the two mirrors. The phase difference will change gradually with moving along the mirror tilt until a completely destructive interference occurs producing a dark fringe at the output. The lines of bright-dark will be repeated

successively, whose periodicity and width depends on the title angle α , or rather the dimension t of the PDMS frame height mismatch. Upon introducing a fluid sample with certain RI (n_s) inside the chamber, the optical path length of the resonator will be changed to $(\ell \cdot n_s)$, causing shift in the interference fringes' pattern. The patterns for the liquid under test and a reference one can be recorded using a digital camera; then the shift between them can be determined by simple image processing, from which the unknown RI value can be evaluated. The light source and camera can be put in close contact with the device without the need for leaving large propagation distance like what is done in Young interferometry techniques, which evades large device sizes. The input collimated monochromatic light is provided by a small size laser diode source.

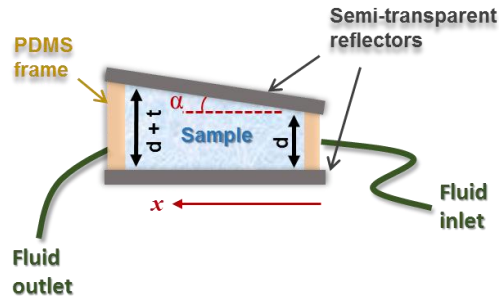


Figure 1. Schematic diagram of the proposed miniaturized wedge interferometer for liquid refractometry.

2.2. Modeling

The analytical modeling of the interference pattern is deduced by treating the structure as a Fabry–Pérot resonator but with varying length ℓ . This approximation is accepted as long as the angle α is small enough to have acceptable round of $\cos(\alpha) \approx 1$; so that the reflection/transmission coefficients and phase difference between the consecutive multiple reflections between the mirrors can be considered nearly the same. The analytical model of the ordinary Fabry–Pérot resonator with parallel mirrors is well developed in literature [21]. Same model can be adopted for the proposed case within successive small intervals along which the resonator distance ℓ can be considered constant within each interval. As for the light beam intensity, the laser beam spot usually has a Gaussian intensity distribution along its cross section. Thereby, the transmission intensity T along distance x can be expressed as in Eq. (1):

$$T = I_0 \left(e^{-\frac{(x-C)^2}{2\sigma^2}} \right) \left(\frac{(1-r)^2}{1+r^2-2r \cos(\varphi)} \right) \quad (1)$$

where I_0 is the maximum intensity, C is the position of the Gaussian beam center, σ is the standard deviation of the Gaussian distribution, r is the mirror reflectance, φ is the phase difference between each succeeding reflection and is equivalent to the formula in Eq. (2):

$$\varphi = \frac{2\pi}{\lambda} 2n_s \ell \cos(\theta) \quad (2)$$

where θ is the angle of the light travels through the resonator, if the light is shined from outside by an incidence angle θ_i . Note that the cavity length ℓ varies along the distance x by the relation $\ell = S.x + d$, where S is the slope of the tilted mirror and is related to the tilt angle α by the relation $S = \tan(\alpha)$. This slope can be easily determined from the separation distance between each two successive fringes or what we can call fringes period (h), as $\Delta\ell = h.S$ in this case and the phase difference $\varphi = 2\pi$. That gives the relation for S as in Eq. (3):

$$S = \frac{\lambda}{2hn_s \cos(\theta)} \quad (3)$$

To evaluate the sensitivity of the device, the amount of the interference fringes shift δx , should be related to the RI change of the solution δn_s . The peak intensity value of the interference fringes occurs at $\varphi = 2\pi m$ where m is an integer. By integrating the previous relation, the sensitivity can be determined by the formula in Eq. (4):

$$\text{Sensitivity} = \frac{\delta n_s}{\delta x} = -\frac{n_s}{\ell} S = \frac{S.n_s}{S.x + d} \quad (4)$$

This model can be used to predict the performance of the sensor with certain design parameters as indicated in Figure 2, which plots the sensitivity versus the cavity length ℓ for different values of the slope S . Logarithmic scale is used for the plot to cover large range. It is explicit that increasing the cavity length ℓ and decreasing the slope S achieves higher performance. For example, slope of 0.001 and a resonator length of 1 cm can theoretically achieves sensitivity of 10^{-7} RIE/ μm , which is better than the state-of-the-art of volume refractometry presented in the introduction, even with much less size. With tolerating longer lengths of few centimeters and smaller slope of 0.0001, beating the state-of-the-art surface refractometer is even possible. But that requires precise dimensions control, implying fabrication by adequate lithography techniques.

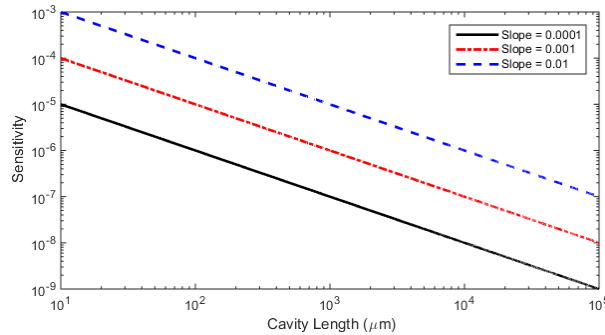


Figure 2. Logarithmic plot for the sensitivity against the cavity length ℓ for different values of the slope S .

2.3. Simulation

To understand the functionality of the demonstrated structure, a scaled-down version of the proposed device has been simulated by HFSS (High Frequency Structure Simulator) software that adopts electromagnetic wave modeling based on finite element method. If the real dimensions were to be simulated, enormous calculation resources would be required. To overcome this problem, miniaturized versions of the structure have been simulated. The simulated structure consists of two reflecting sheets of area $2.5 \mu\text{m} \times 4.5 \mu\text{m}$, separated by distance $d = 2.7 \mu\text{m}$ at the origin, and the upper reflector is tilted by an angle $\alpha = 9^\circ$ which introduces an increment of separation distance $t = 0.7 \mu\text{m}$ at the other end. The reflectors are formed by dielectric sheet of high RI value equal to 3.5 and thickness of 38.2 nm equivalent to quarter wavelength of the excitation wave that is a plan wave of $\lambda = 532 \text{ nm}$. The volume between the two reflectors is filled with a medium of RI values n_s equal to 1.02, then 1.04. The difference in refractive indices filling the device causes shifts in the positions of the fringes at the output of the device. Figure 3 (a) and (b) shows the irradiance viewed on a screen put just outside the structure in the two cases of $n_s = 1.02$ and 1.04 respectively.

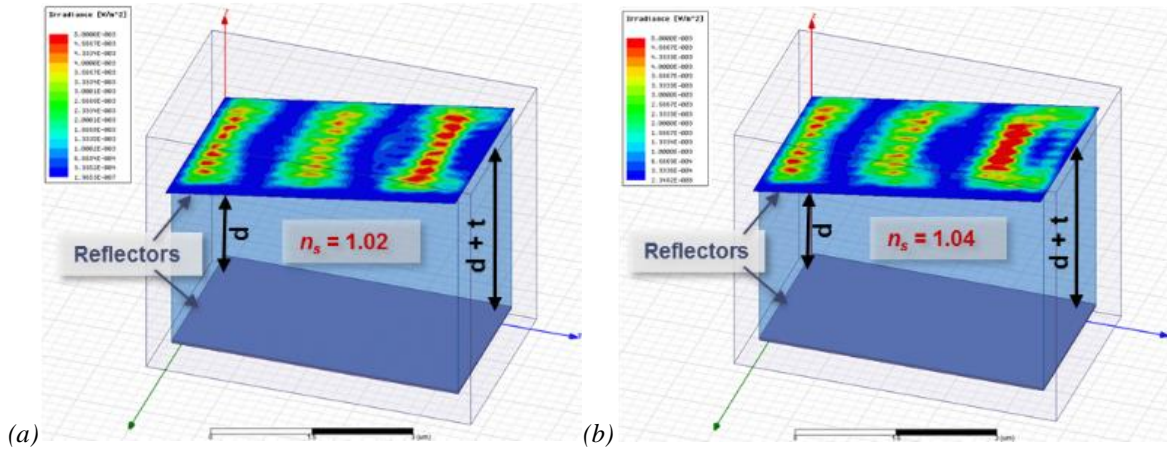


Figure 3. FEM Simulations for the irradiance at the output from a scaled-down model of the wedge interferometer filled with fluids of RI (a) $n_s = 1.02$ (b) $n_s = 1.04$.

The fringes shift can be noticed clearly in Figure 4 that shows a plot for the normalized irradiance in the two cases plotted along a line in the same plan of the viewing screen extended along the Y direction. It can be noticed from the plot that the shift between the peaks increases with the distance as the separation between the two reflectors increases; which is equivalent to increasing the sensitivity as previously demonstrated in Figure 2. Note that the sensitivity here is much less than the real case with large dimensions as the simulated case has much smaller dimensions to fit the limited simulation volume.

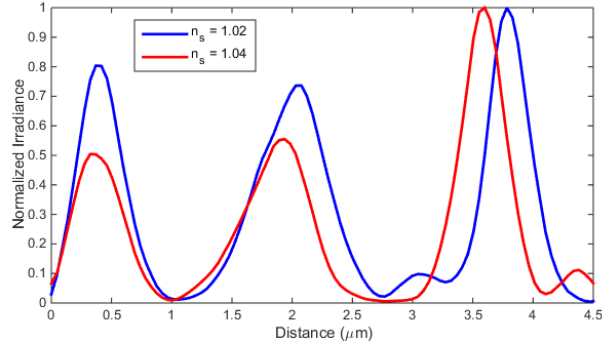


Figure 4. Normalized smoothed irradiance extracted from simulations in figure 3, plotted against distance.

3. Experimental

3.1. Device fabrication

The semi reflecting mirrors are fabricated by sputtering about 60 nm of Aluminum on cleaned glass slide covers of size 22×22 mm. The thin Aluminum layer reflectivity was experimentally measured to be about 85% using a collimated green laser source at wavelength 532 nm. The chamber is fabricated by mixing the PDMS gel with its curing agent by ratio 10:1 weight/weight (w/w) and pour it into a petri dish that is left for curing on an optical table to ensure flat leveling. The dish is elevated from one side by putting beneath it a glass slide (thickness 1.1 ± 0.5 mm) to produce variable thickness PDMS film number 1 with certain tilt angle. This film is used to fabricate the refractometer number 1. Another PDMS film number 2 has a different tilt angle is produced by elevating the petri dish while curing the PDMS gel by a glass slide cover (thickness 0.15 ± 0.2 mm), that is used to fabricate refractometer number 2. The PDMS is left to cure in the ambient temperature for two days to avoid air bubbles formation if rapidly cured at high temperature. After curing, the PDMS is peeled of the molding dish and cut in square pieces of size equivalent to the mirrors size, and an opening is cut inside each piece to produce a space for the liquid sample to fill. Two fluidic tubes are connected through the frame for sample delivery and disposal. Then finally, the two mirrors are bonded from top and bottom of the PDMS frame.

A green laser pointer with a good collimated beam has been used to illuminate the device, and the produced interference patterns is recorded by a CCD camera with pixel pitch of 2.2 μm. The pattern captured for empty device is used to accurately determine the dimensions and title angle of the structure. Then 5% (w/v) Glucose pharmaceutical solution is diluted by DI-water with different ratios to prepare test samples that are used for the refractometry functional evaluation.

3.2. Results and Discussion

The fringes' images captured for empty (filled with air) device 1 and device 2 are presented in Fig. 5 (a) and (b) respectively. Multi-spots appears as the input beam is shined on the device with a small incidence

angle. This angle is practically useful to separate the multi-reflected spots between the two mirrors from each other, otherwise they all will coincide producing a complex interference pattern that is very challenging to resolve.

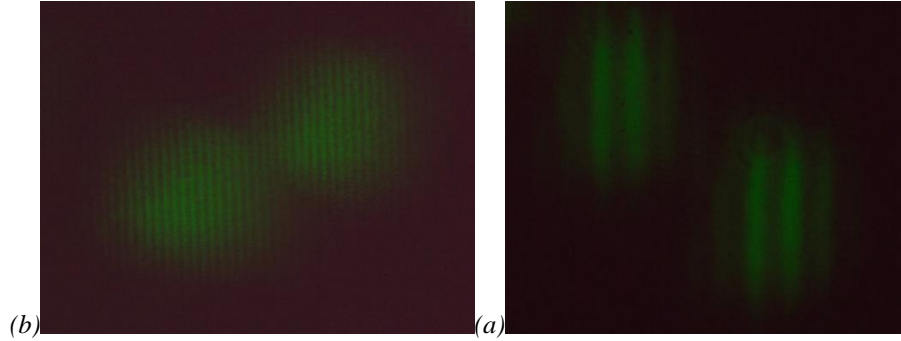


Figure 5. Interference fringes captured by a CCD camera in case of air for (a) device 1 (b) device 2.

By analyzing the captured images using the image processing software ‘ImageJ’, the green color intensities are resolved and analyzed giving the pattern of the interference fringes. The normalized intensity values along the lateral direction are plotted in Figure 6. The periodicity of the fringes h is obtained by performing FFT (Fast Fourier Transform) processing for the pattern; from which, the slope S can be determined from equation 3. This rough estimation is used as a seed for iterative calculation of the transmission T presented in equation 1 to simulate the interference pattern. The values for the slopes which give the best fitting with the measured patterns for device 1 and device 2 are 0.00475 and 0.00123 respectively. That corresponds to tilting angles α of 0.27° and 0.7° respectively. Figure 6 shows the simulation compared to the measurement extracted from the images in Figure 5.

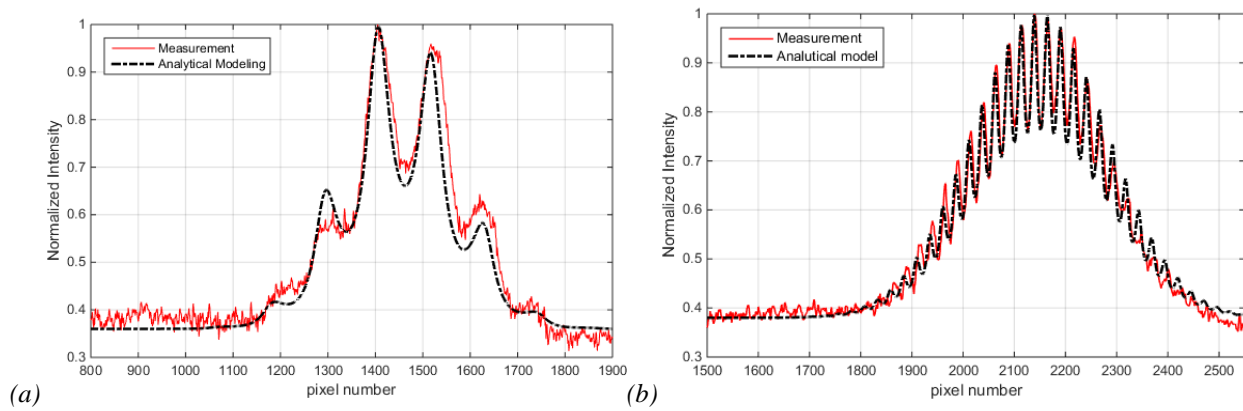


Figure 6. The normalized intensity for the green color of the middle spot in the interference pattern for DI-water, compared with the simulation modeling.

For the refractometry experimental testing, device 1 is filled with DI-water, then with Glucose aqueous solution with concentrations of 0.1% and 0.15%. The interference fringes pattern is captured by the CCD camera in each case. The obtained images are analyzed by image processing to extract the interference patterns. Figure 7 shows the normalized intensity of the fringe patterns for all cases. The evident spatial shift between them corresponds to the change in RI of each solution.

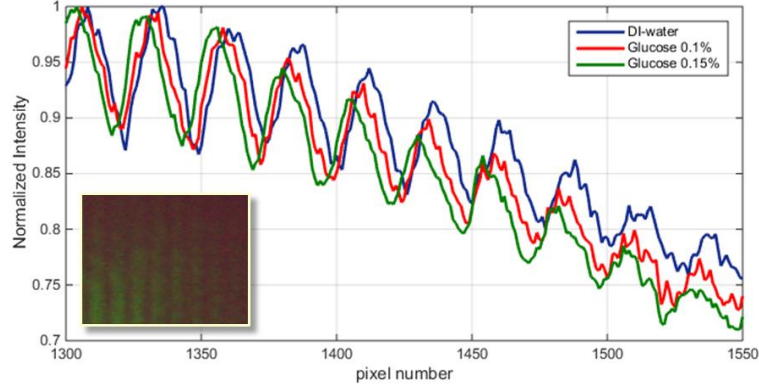


Figure 7. The interference patterns for DI-water and glucose with different concentration. The inset shows the image of the interference fringes in case of DI-water.

From the analysis of the patterns in Figure 7, the interference fringes' shifts with changing glucose concentrations has been determined from all the peaks. The mean and standard deviation (σ_e) of the data are calculated and plotted on the left hand side axis in Figure 8. The mean values are represented by the blue circles and the error bars represent $\pm \sigma_e$. Theoretical RI values for the glucose solution of concentration 0.5% are obtained from literature [22]. The relation between RI and glucose concentration is assumed to be linear within the lower concentrations range and is plotted on the right hand side axis in Figure 8 represented by the red line.

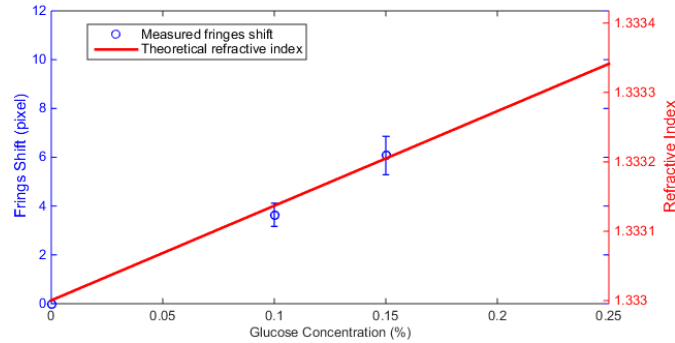


Figure 8. The interference fringes' shifts with changing glucose concentrations on the left hand side axis (blue colored), and the theoretical refractive index values on the right hand side axis (red colored). Error bars represents the standard deviation (σ_e) calculated from the interference fringes' shifts for all the peaks in Figure 7.

The graph of Figure 8 is used to estimate the sensitivity of the device that is found to be 3.65×10^{-5} RIE/pixel. This value depends on the pixel size of the CCD camera in use, and can be enhanced by using smaller pixel size. To avoid this dependence, the shift per length can be employed which will be 1.66×10^{-5} RIE/ μm . The resolution of a sensor is estimated by three times the root mean square value (rms) of the noise variations, that is the standard deviation σ_e [23]. From the error bars in Figure 8, the maximum standard deviation is

0.79 *pixel*, then the resolution $3\sigma_e = 2.37$ *pixel*. The Detection Limit of a refractometer is the smallest change in RI that can be accurately detected. Then for the presented detector, it can be obtained by multiplying the above stated sensitivity by the resolution; which results in 8.7×10^{-5} RIE.

4. Conclusions

In this paper, successful proof of concept has been demonstrated for a novel miniaturized refractometer based on wedge interferometry. Analytical modeling for the structure, numerical simulations and experimental results has been presented. A compact size laboratory prototype has been fabricated by a simple and cheap fabrication method that is based on PDMS casting without any lithography and semitransparent mirror fabricated by thin film Aluminum sputtering on glass. Sensitivity of 3.65×10^{-5} RIE/*pixel* has been achieved for glucose concentration detection, with Detection Limit up to 8.7×10^{-5} RIE. In the future work, microfabrication techniques will be used for fabricating more demanding design parameter achieving better performance and more compact size. Integrated laser source and camera of a smart phone are suggested for further reduction of the device size, which is appealing for hand-held test devices.

Acknowledgment. The author would like to acknowledge Mahmoud Ameen, Aboul Wafa Singer, Ramy Yassin from the cleanroom engineers team for their support in the device fabrication.

References

1. D. L. Kenneth, Y. Hojeong, and T. C. Brian “Smartphone instrument for portable enzyme linked immunosorbent assays,” *Biomed. Opt. Express* **5**, 3792-3806 (2014).
2. X. Fan, and I. M. White, “Optofluidic microsystems for chemical and biological analysis,” *Nature Photonics* **5**, 591–597 (2011).
3. D. Psaltis, S. R. Quake, and C. Yang, “Developing optofluidic technology through the fusion of microfluidics and optics,” *Nature* **442**, 381–386, (2006).
4. Q. Liu, H. J. Huang, L. K. Chin, Y. F. Yu, and X. C. Li “Label-free detection with micro optical fluidic systems (MOFS): a review,” *Anal. Bioanal. Chem.* **39**, 2443-2452 (2008).
5. M. E. Gertsenshtein, and V. I. Pustovoit “On the Detection of Low-Frequency Gravitational Waves,” *Sov. Phys. JETP* **16**, 433-435 (1963).
6. B. P. Abbott, et al. “Observation of Gravitational Waves from a Binary Black Hole Merger,” *Phys. Rev. Lett.* **116**, 061102 (2016).

7. P. R. Saulson "Physics of Gravitational Wave Detection: Resonant and Interferometric Detectors," in Proceedings of the XXVIth SLAC Summer Institute, Stanford, CA, USA, (1998), pp. 113-162.
8. K. Schmitt, B. Schirmer, C. Hoffmann, A. Brandenburg, P. Meyrueis, "Interferometric biosensor based on planar optical waveguide sensor chips for label-free detection of surface bound bioreactions," *Biosens. Bioelectron.* **22**, 2591–2597 (2007).
9. K. Chaitavon, S. Sumriddetchkajorn, and J. Nukeawb, "Highly sensitive refractive index measurement with a sandwiched single-flow-channel microfluidic chip," *RSC Adv.* **3**, 6981-6984 (2013).
10. A. Ymeti, J. S. Kanger, J. Greve, P. V. Lambeck, R. Wijn, and R.G. Heideman, "Realization of a multichannel integrated Young interferometer chemical sensor," *Appl. Optics* **42**, 5649-5660 (2003).
11. A. Brandenburg, "Differential refractometry by an integrated-optical Young interferometer," *Sens. Actuators B* **38**, 266–271 (1997).
12. D. Yuan, Y. Dong, Y. Liu, and T. Li, "Mach-Zehnder Interferometer Biochemical Sensor Based on Silicon-on-Insulator Rib Waveguide with Large Cross Section," *Sensors* **15**, 21500-21517 (2015).
13. F. Prieto, et al. "An integrated optical interferometric nanodevice based on silicon technology for biosensor applications," *Nanotechnology* **14**, 907–912 (2003).
14. D. Yuan, Y. Dong, Y. Liu and T. Li, "Design of a High-Performance Micro Integrated Surface Plasmon Resonance Sensor Based on Silicon-On-Insulator Rib Waveguide Array," *Sensors* **15**, 17313-17328 (2015).
15. R. Ramponi, M. Marangoni, R. Osellame, *Optical Waveguide Refractometers*. In: S. Martellucci, A.N. Chester, A.G. Mignani (eds) *Optical Sensors and Microsystems*. (Springer, Boston, MA, 2002).
16. R. Guider, D. Gandolfi, T. Chalyan, L. Pasquardini, A. Samusenko, C. Pederzoli, G. Pucker, and L. Pavesi, "Sensitivity and Limit of Detection of biosensors based on ring resonators," *Sens. Biosensing Res.* **6**, 99-102 (2015).
17. S. Arnold, D. Keng, S. I. Shopova, S. Holler, W. Zurawsky, and F. Vollmer "Whispering gallery mode carousel – a photonic mechanism for enhanced nanoparticle detection in biosensing," *Opt. Express* **17**, 6230-6238 (2009).
18. H. M. Shabana, "Determination of film thickness and refractive index by interferometry," *Polymer Testing* **23**, 695–702 (2004).

19. M. W. Pruessner, T. H. Stievater, and W. S. Rabinovich, "In-plane microelectromechanical resonator with integrated Fabry–Pérot cavity," *Appl. Phys. Lett* **92**, 081101 (2008).
20. F. Marty, L. Rousseau, B. Saadany, B. Mercier, O. Francais, Y. Mita, T. Bourouina, "Advanced etching of silicon based on deep reactive ion etching for silicon high aspect ratio microstructures and three-dimensional micro- and nanostructures," *Microelectronics Journal* **36**, 673–677 (2005).
21. G. Hernandez, *Fabry–Pérot Interferometers* (Cambridge University Press, 1986).
22. D. R. Lide, *CRC Handbook of Physics and Chemistry* (CRC Press, 2004).
23. I. M. White, and X. Fan, "On the performance quantification of resonant refractive index sensors," *Opt. Express* **16**, 1020-1028 (2008).